Composites Part B 220 (2021) 108995

Contents lists available at ScienceDirect

Composites Part B

journal homepage: www.elsevier.com/locate/compositesb

Gram-scale synthesis of rGO wrapped porous α-Fe_2O_3 as an advanced anode material for Na-ion batteries with superior cyclic stability

Syam Kandula [a], Junho Bae [b], Jinhan Cho [c], Jeong Gon Son [a,c,*]

[a] Soft Hybrid Materials Research Center, Korea Institute of Science and Technology, 5 Hwarang-ro 14-gil, Seongbuk-gu, Seoul, 02792, Republic of Korea
[b] Department of Chemistry, Seoul National University, 1 Gwanak-ro, Gwanak-gu, Seoul, 08826, Republic of Korea
[c] KU-KIST Graduate School of Converging Science and Technology, Korea University, 145 Anam-ro, Seongbuk-gu, Seoul, 02841, Republic of Korea

ARTICLE INFO

Keywords:
α-Fe_2O_3@rGO core@shell nanocubes
Economical approach
Sodium-ion batteries (SIBs)
Electrode materials
Energy storage devices
Specific capacity

ABSTRACT

Synthesis of various earth-abundant electroactive materials in gram-scale via simple methods with excellent efficiency can effectively reduce the cost. In this context, we have demonstrated a gram-scale synthesis of α-Fe_2O_3@rGO core@shell nanocubes via a direct solution route. By the concept of charge-charge interactions, we have successfully wrapped the reduced graphene oxide (rGO) over the surface of α-Fe_2O_3 nanocubes resulting in the formation of α-Fe_2O_3@rGO core@shell nanocubes in a gram-scale. The synthesized α-Fe_2O_3@rGO core@shell nanocubes were characterized by a group of analytical methods and finally explored as an effective anode material for sodium-ion batteries (SIBs). The α-Fe_2O_3@rGO-10 wt% core@shell nanocubes sample displays an exceptional specific capacity of 970.2 mAh g^{-1} at 0.1 C-rate with a better rate capability of 77.8 mAh g^{-1} at 5.0 C-rate. Moreover, the α-Fe_2O_3@rGO-10 wt% sample also demonstrates a better specific capacity of about 586.9 mAh g^{-1} after 100 cycles at 0.1 C-rate. The current approach can enable the synthesis of various electroactive materials on a gram-scale using a cost-effective strategy with better electrochemical performance for practical energy storage devices.

1. Introduction

Energy scarcity is the main problem shortly because of the rapid consumption of natural fossil fuels, resulting in an exponential increase in global warming and severe environmental issues [1,2]. Various alternative sustainable energy technologies, such as wind, solar, hydrogen energy, etc., have been regulated to solve this problem [3,4]. The intermittent nature of these resources restricts their large-scale utilization as reliable power sources. The current era is mainly concentrating on the electrification of vehicles and smart power grids [5,6]. The development of highly efficient and economical energy conversion and storage devices attracts a keen interest for their commercialization. In this context, lithium rechargeable batteries (LIBs) have been shown a sound output in high energy density, low self-discharge, long life, minimum maintenance, and eco-friendliness [7,8]. However, uneven distribution and the low affluence of lithium supplies in the earth crust doubt the development of efficient energy technologies in the future [9,10]. In recent years, SIBs are considered one of the alternatives for LIBs because of their high abundance, high safety, economic, and the most important fact is the charge storage mechanism is similar to LIBs [11]. However, the larger atomic radius of Na^+ (1.02 Å) than that of Li^+ (0.76 Å) hinders faster reaction kinetics in SIBs, resulting in significant volume changes, especially in anode electrode materials [12,13].

To date, various materials such as carbonaceous compounds, metal oxides/nitrides/sulfides/phosphides, and metal alloys have been explored as anode materials for SIBs [14–17]. Most of these materials alone suffer from low conductivity or significant volume expansion leading to poor cyclic stability. Various strategies have been established to control these problems, including doping of foreign elements into the crystal lattice of active material, tuning nanostructure morphology, forming composite materials, etc. [18]. In recent years, various metal oxides have been explored as anode materials for SIBs. Fe_2O_3 has paid more attention to these metal oxides because of their natural abundance, high chemical constancy, economical, and eco-friendliness [12,13]. Furthermore, it also exhibits a high theoretical specific capacity of 1007 mAh g^{-1} [6]. Nevertheless, Fe_2O_3 alone struggles with a significant volume expansion during the cyclic stability causes pulverization of the electrode. Fe_2O_3 has been combined with various carbonaceous

* Corresponding author. Soft Hybrid Materials Research Center, Korea Institute of Science and Technology, 5 Hwarang-ro 14-gil, Seongbuk-gu, Seoul, 02792, Republic of Korea.
E-mail address: jgson@kist.re.kr (J.G. Son).

https://doi.org/10.1016/j.compositesb.2021.108995
Received 27 February 2021; Received in revised form 11 May 2021; Accepted 11 May 2021
Available online 17 May 2021

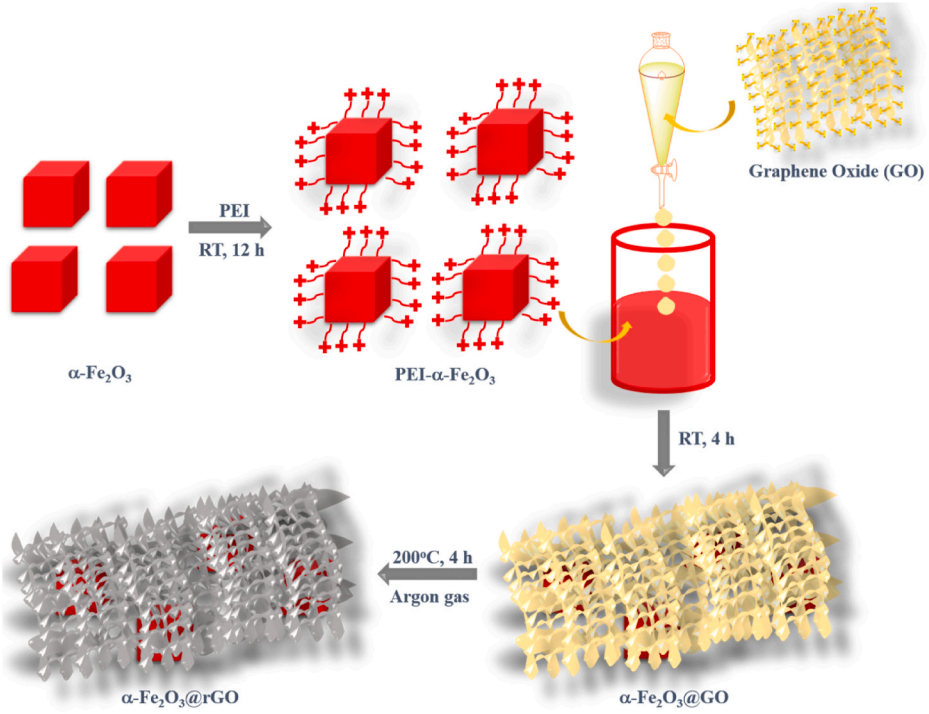

Scheme. 1. A schematic illustration for the synthesis of α-Fe_2O_3@rGO core@shell nanocubes.

materials or doping with foreign elements to solve these issues [19,20]. For example, Zhang et al. have produced the α-Fe_2O_3/rGO nanocomposites by microwave synthesis and examined them for SIBs [12]. They have exhibited a specific capacity of about 890.0 mAh g^{-1} at a current density of 0.1 mA g^{-1}, but they have reserved only 310.0 mAh g^{-1} after 150 cycles [12]. Liu et al. have synthesized the Fe_2O_3/rGO nanocomposites, which has displayed a low specific capacity (390.0 mAh g^{-1}) at a low current density (0.05 mA g^{-1}) [21]. Li et al. have grown the Fe_2O_3 single crystallites on rGO; it has demonstrated a specific capacity of 610.0 mAh g^{-1} at a current density of 0.05 mA g^{-1} and has retained a specific capacity of 500.0 mAh g^{-1} after 100 cycles at the same current density [22]. Li et al. have synthesized the amorphous Fe_2O_3/graphene composite nanosheets, which have shown a specific capacity of about 440.0 mAh g^{-1} at a current density of 0.1 mA g^{-1} [23]. It has also demonstrated a better initial coulombic efficiency (CE) of approximately 81.2%, indicating an essential role of graphene to enhance its initial CE. Kong et al. have prepared the α-Fe_2O_3 nanorod arrays on rGO, which has demonstrated a specific capacity of about 350.0 mAh g^{-1} at a current density of 0.2 mA g^{-1}. It has retained a stable capacity of 332.0 mAh g^{-1} after 300 cycles, indicating the advantage of 1D growth of α-Fe_2O_3 nanorod arrays on rGO for better Na-ion storage through synergistic channels [13]. Meng et al. have explored the Fe_2O_3/nitrogen-doped graphene nanosheets for SIBs; it has displayed a specific capacity of about 401.0 mAh g^{-1} at a current density of 0.05 mA g^{-1} and has retained about 306.0 mAh g^{-1} after 50 cycles at the same current density [24]. Recently, Wang et al. have demonstrated the Fe_2O_3/N, S co-doped modified graphene for SIBs, which has displayed a specific capacity of 467.0 mAh g^{-1} after 50 cycles at 0.1 A g^{-1} [20]. The formation of amorphous composite structures, growing single crystallites, tuning of Fe_2O_3 structure, and doping of foreign elements into graphene have been explored [12,13,20–24]. However, they have still lacked the theoretical specific capacity and better stability of the composite materials.

We have demonstrated the gram-scale synthesis of various amounts of rGO-wrapped porous α-Fe_2O_3 core@shell nanocubes via a simple solution route in the present study. The α-Fe_2O_3@rGO core@shell nanocubes possess several advantages, which includes as follows: (i) the current method offers the synthesis of uniform α-Fe_2O_3 nanocubes contain many pores on its surface via an economical route with an excellent yield (~150.0 g) in a single step; the high yield of α-Fe_2O_3 nanocubes allows us to make a gram-scale synthesis of α-Fe_2O_3@rGO nanocomposites via simple chemistry further, which is more economical as well as efficient for battery fabrication; (ii) the porous structure of α-Fe_2O_3 enables a high number of active sites for Na-ion storage, and also it can hold significant volume changes throughout the cycling studies; and (iii) the rGO outer layers can shorten the diffusion length of Na-ion as well as protect the porous α-Fe_2O_3 nanocubes from rapid degradation across the charge/discharge cycles. The α-Fe_2O_3@rGO core@shell nanocubes were explored as an anode material for SIBs, and among them, the α-Fe_2O_3@rGO-10 wt% sample displays a specific capacity of about 970.2 mAh g^{-1} at a C-rate of 0.1C with a good rate capability of 77.8 mAh g^{-1} at a high C-rate of 5.0C (50 times than the initial C-rate). Moreover, the α-Fe_2O_3@rGO-10 wt% sample exhibits better cyclic stability of about 587.0 mAh g^{-1} (~60.5% of initial specific capacity) after 100 cycles at a C-rate of 0.1C. The better specific capacity and cyclic stability mainly contribute to the efficient synergistic interaction between the porous α-Fe_2O_3 nanocubes and rGO nanosheets.

2. Experimental section

2.1. Reagents

Iron(III) chloride hexahydrate (≥97.0%, Sigma-Aldrich), sodium hydroxide pellets (≥97.0%, Daejung Chemicals & Metals), polyethyleneimine (branched, M_w ~ 25,000, Sigma-Aldrich), graphite powder (<20 μm, Sigma-Aldrich), potassium permanganate (≥97.0%, Sigma-Aldrich), hydrogen peroxide solution (30.0 wt%, Sigma-Aldrich), and sulfuric acid (≥98.0%, Daejung Chemicals & Metals, Korea) were purchased and used as received.

2.2. Synthesis

The synthesis of α-Fe_2O_3@rGO core@shell nanocubes was carried out in three steps. The synthetic details are as follows.

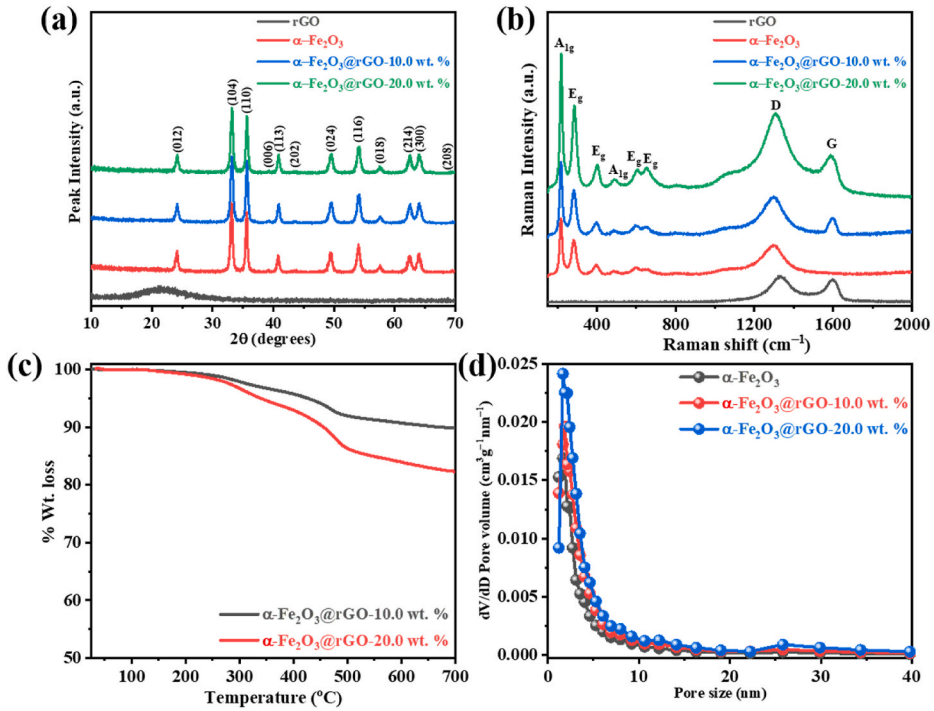

Fig. 1. (a) XRD, and (b) Raman plots of rGO, α-Fe_2O_3, and α-Fe_2O_3@rGO core@shell nanocubes, (c) TGA plot of α-Fe_2O_3@rGO core@shell nanocubes, and (d) BJH plot of α-Fe_2O_3, and α-Fe_2O_3@rGO core@shell nanocubes.

2.3. Synthesis of the α-Fe_2O_3 nanocubes

The α-Fe_2O_3 nanocubes were synthesized by a well-known sol-gel method. Initially, 2.0 M Iron(III) chloride hexahydrate ($FeCl_3.6H_2O$) solution was prepared in a 1.0 L of de-ionized (DI) water in a glass bottle and kept under constant stirring at room temperature until dissolving the iron salt. Then, a 5.4 M sodium hydroxide (NaOH) aqueous solution was prepared in 1.0 L of DI water. This solution was mixed to the above-prepared solution at a constant stirring by dropwise at room temperature and continued the stirring further for another 30 min. The obtained thick gel was transferred into a preheated oven at 100 °C and continued reaction for eight days by aging. After completing the reaction, a reddish-brown precipitate was gathered by a repeated centrifuge and washed with distilled water and ethanol several times. The sample was dried at 100 °C overnight under a vacuum oven to attain the α-Fe_2O_3 nanocubes powder sample (150.0 g).

2.4. Synthesis of surface modification of the α-Fe_2O_3 nanocubes

About 20.0 g of α-Fe_2O_3 nanocubes were dispersed in 1.0 L of distilled water and sonicated for about 5 min to get a uniform dispersion. After that, 20.0 g of polyethyleneimine (PEI) was dissolved in 2.0 L of distilled water and added this solution to the above dispersion at a constant stirring at room temperature. This mixture was stirring for overnight at room temperature. The obtained residue was centrifuged and washed with DI water and ethanol. The sample was finally dried in the vacuum oven overnight to get surface-modified α-Fe_2O_3 nanocubes.

2.5. Synthesis of the α-Fe_2O_3@rGO core@shell nanocubes

Graphene oxide (GO) was produced based on our previous reports [25,26]. Various amounts of GO (e.g., 0.5 g or 1.0 g in 0.5 L of DIW) were added in a dropwise passion to the suspension of about 5.0 g of surface-modified α-Fe_2O_3 nanocubes in a 2.5 L of an aqueous solution. The contents were stirred for 4 h at room temperature, and the collected residue was centrifuged, washed with distilled water and ethanol. The powder samples were calcined at 200 °C for 4 h under an argon atmosphere (200 SCCM) to get α-Fe_2O_3@rGO core@shell nanocubes. The final samples were labeled as α-Fe_2O_3@rGO-10 wt% and α-Fe_2O_3@rGO-20 wt% corresponding to 0.5 g and 1.0 g of GO, respectively. The digital images of these samples are shown in Fig. S1.

2.6. Results and discussion

The formation of α-Fe_2O_3@rGO core@shell nanocubes is displayed in Scheme 1. Initially, iron salt ionizes to Fe^{2+}, which reacts with the hydroxide ions leading to $Fe(OH)_3$. At 100 °C, the formed product undergoes phase transformation by dehydration and produces α-Fe_2O_3 nanocubes [27]. Afterward, the surface of α-Fe_2O_3 nanocubes is modified with a PEI at room temperature, resulting in a positive charge over the surface of α-Fe_2O_3 nanocubes. Then, with the help of charge-charge interactions, negatively charged GO sheets are wrapped on the surface of positively charged α-Fe_2O_3 nanocubes. Finally, calcination under an argon atmosphere resulting in the formation of α-Fe_2O_3@rGO core@-shell nanocubes. The crystal structure of rGO, α-Fe_2O_3, and α-Fe_2O_3@rGO core@shell nanocubes were studied using XRD analysis as displayed in Fig. 1a. The pure rGO sample shows a broad diffraction peak centered at about 24.5° and a very weak diffraction peak centered at about 42.8°, conforming to (002) and (100) planes of graphene. The XRD patterns of pure α-Fe_2O_3 and α-Fe_2O_3@rGO core@shell samples exhibit the significant reflections at a 2θ of 24.2, 33.2, 35.6, 40.8, 49.5, 54.2, 57.6, 62.6, and 64.0° corresponding to (012), (104), (110), (113), (024), (116), (018), (214), and (300), and three minor reflections at 39.2, 43.5, and 69.4° corresponding to (006), (202), and (208) reflections of Fe_2O_3 (JCPDS No. 33–0664), respectively. In the case of α-Fe_2O_3@rGO core@shell samples, no significant XRD reflections of rGO are noticed, indicating the amorphous nature of rGO in these samples. The crystallite size of α-Fe_2O_3 in these samples was estimated using a Debye-Scherrer equation at 2θ of 33.2°, and it is expressed as follows.

$$\delta = \frac{K\lambda}{\beta Cos\theta} \quad (1)$$

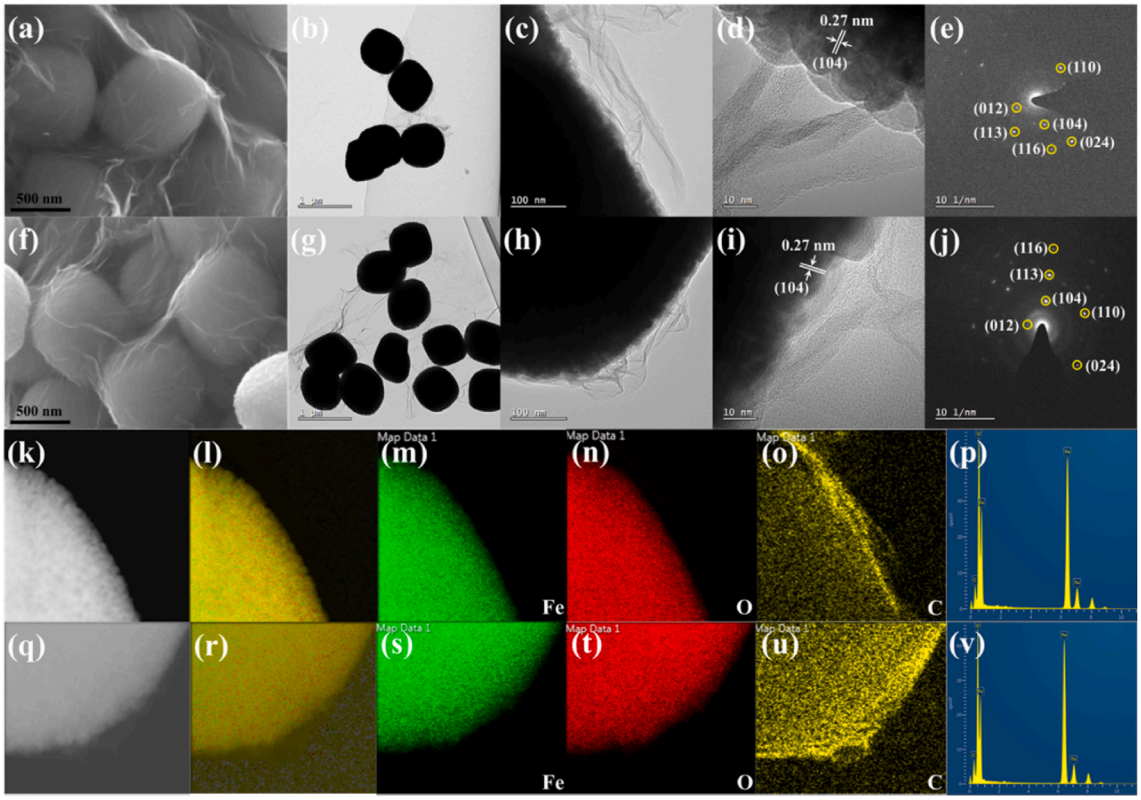

Fig. 2. (a, f) FE-SEM, (b, g) low-magnification TEM, (c, h) high-magnification TEM, (d, i) HRTEM, (e, i) SAED, (k-o, q-u) EDS color mapping, and (p, v) EDS spectra of α-Fe_2O_3@rGO-10 wt% and α-Fe_2O_3@rGO-20 wt% core@shell nanocubes, respectively. (For interpretation of the references to color in this figure legend, the reader is referred to the Web version of this article.)

Here δ is the average crystallite size of nanoparticles (nm), K is a dimensionless parameter (0.89), λ is the wavelength of Cu-K_α X-ray radiation, β is the full-width half-maximum, and θ is the Bragg angle. Crystallite size was calculated to be 19.3, 19.1, and 19.0 nm for the α-Fe_2O_3, α-Fe_2O_3@rGO-10 wt%, and α-Fe_2O_3@rGO-20 wt% samples, respectively. These results are indicating the phase purity of Fe_2O_3 in the α-Fe_2O_3@rGO core@shell nanocubes without any impurities. Moreover, coating of rGO over the surface of α-Fe_2O_3 nanocubes doesn't change the crystallite size of Fe_2O_3 in the α-Fe_2O_3@rGO core@shell nanocubes.

Raman spectroscopy was carried out to enumerate the existence of rGO in these samples, and the corresponding results are shown in Fig. 1b. In a Raman spectroscopy, *zz* polarization allows A_{1g} modes, crossed *xz,* and *yz* polarization allows E_g modes, while the polarization in *xx* and *xy* configuration allows magnon scattering [28,29]. The α-Fe_2O_3 and α-Fe_2O_3@rGO core@shell nanocubes display two sets of Raman bands. One set of bands at 218.0, and 487.0 cm^{-1} correspondings to A_{1g} mode, while the other set of bands at 280.0, 395, 605, and 653 cm^{-1} ascribed to E_g mode of α-Fe_2O_3 [13]. Interestingly, the broadband at 653 cm^{-1} in these samples mainly attributes to the formation of disordered hematite by dehydration [29]. Another two broad bands centered at 810 and 1057 cm^{-1} mainly attribute to polarization in *xx* direction because of first-order magnon scattering [28,30]. In addition, another broadband at about 1300 cm^{-1} in the α-Fe_2O_3 sample indicates the characteristic mode of hematite, which can be ascribed to the interaction of two-magnon scattering on antiparallel close spin sites [12, 28]. In α-Fe_2O_3@rGO core@shell nanocubes, the characteristic band of hematite at 1300 cm^{-1} is merged with the D band of rGO, while another band, 1590 cm^{-1}, consistent with the G band of rGO [12]. Among the α-Fe_2O_3@rGO core@shell nanocubes, α-Fe_2O_3@rGO-10 wt % sample shows a higher I_D/I_G value (1.74) than that of α-Fe_2O_3@rGO-20 wt % sample (1.55) indicating a more disordered porous structure of carbon, promising for better Na-ion storage since the more disordered or defected rGO structure possesses vacant sites that could enhance the electron and ion transport pathway channels [31,32].

To estimate the carbon (rGO) content in the α-Fe_2O_3@rGO core@shell nanocubes, thermogravimetric analysis (TGA) was conducted under air, and the related plot is shown in Fig. 1c. The total weight loss at 700 °C is about 10.1 and 17.8%, corresponding to α-Fe_2O_3@rGO-10 wt% and α-Fe_2O_3@rGO-20 wt% samples. Until 250 °C, the α-Fe_2O_3@rGO core@shell nanocubes don't show any weight loss. A significant weight loss between 250 and 500 °C is ascribed to the pyrolysis of rGO under air in the samples [12,13,33]. The specific surface area (SSA) and pore size distribution exhibit a vital part in the electrochemical accomplishment of the electrode materials. The SSA of the α-Fe_2O_3 and α-Fe_2O_3@rGO core@shell nanocubes was assessed using Brunauer-Emmet-Teller (BET) analysis (Fig. S2), and all the samples exhibit a characteristic type-IV curve with H3 hysteresis. The SSA of the samples is measured to be 39.4, 47.6, and 51.8 $m^2\ g^{-1}$ corresponding to α-Fe_2O_3, α-Fe_2O_3@rGO-10 wt% and α-Fe_2O_3@rGO-20 wt%, respectively. The pore size distribution was estimated according to the BJH method, and the corresponding outcomes are provided in Fig. 1d. The pore size of the samples is measured to be 1.66, 1.88, and 1.72 nm corresponding to α-Fe_2O_3, α-Fe_2O_3@rGO-10 wt%, and α-Fe_2O_3@rGO-20 wt%, respectively. The narrow pore size distribution indicates well-defined mesopores, which favors better Na-ion storage [2].

The morphology of the α-Fe_2O_3 and α-Fe_2O_3@rGO core@shell nanocubes were analyzed using FE-SEM and TEM analysis (Figs. 2 and S3). The FE-SEM image of the α-Fe_2O_3 sample shows uniformly distributed cubic shape morphology with soft edges and corners (Fig. S3a). Moreover, the α-Fe_2O_3 nanocubes indicate a rough surface with smaller pores on its surface, ascribed to the aggregation of smaller α-Fe_2O_3 nanoparticles leading to α-Fe_2O_3 nanocubes. The presence of pores on the surface of α-Fe_2O_3 nanocubes can allow the free shuttling of

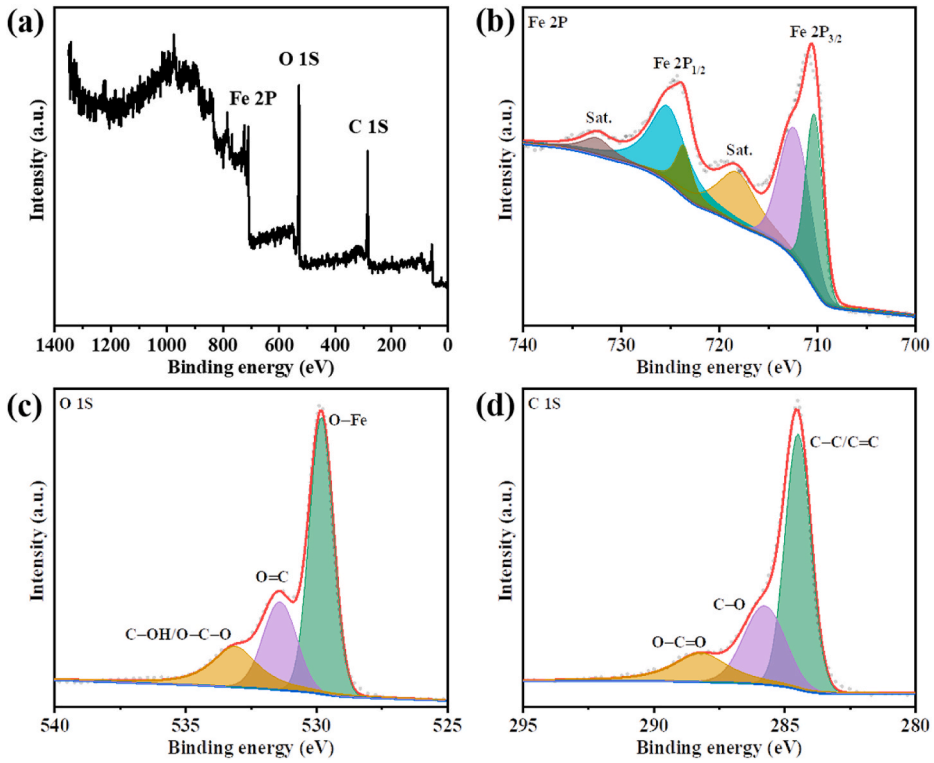

Fig. 3. (a) XPS survey spectrum, and (b–d) high-resolution XPS spectra of Fe2p, O1s, and C1s of α-Fe_2O_3@rGO-10 wt% core@shell nanocubes.

Na-ions during the GCD cycles, which favors the accommodation of volume changes. The diameter of the α-Fe_2O_3 nanocubes is estimated to be about 500 ± 20 nm. The surface-modified α-Fe_2O_3 nanocubes also exhibit similar morphology to α-Fe_2O_3 nanocubes without any change (Fig. S3b). The FE-SEM images of α-Fe_2O_3@rGO core@shell nanocubes are displayed in Fig. 2a and f. They can clearly show the complete wrapping of rGO monolayer sheets over the surface of α-Fe_2O_3 nanocubes with many folds and crumples. The 3D interconnected network between the α-Fe_2O_3 nanocubes and the rGO layers favors better Na-ion insertion and deinsertion by shortening the diffusion path length during the GCD cycles. Three-dimensionally connected rGO shell can accommodate volume changes offered by α-Fe_2O_3 nanocubes during the GCD cycles (Fig. S4). Moreover, the rGO shell effectively protects the aggregation of α-Fe_2O_3 nanocubes upon long-term cycling.

To better understand the morphology of α-Fe_2O_3@rGO core@shell nanocubes, TEM analysis was carried out, and high/low magnification TEM images are given in Fig. 2b and c and Fig. 2g and h, corresponding to α-Fe_2O_3@rGO-10 wt% and α-Fe_2O_3@rGO-20 wt% samples, respectively. Fig. 2c and h indicate an interface between the α-Fe_2O_3 nanocubes and the rGO shell layers. A rough surface of α-Fe_2O_3 nanocubes with gaps between each surface particle is noticed, which favors easy insertion and deinsertion pathways for Na-ions via conductive rGO network. Fig. 2d and i indicating HRTEM images of the α-Fe_2O_3@rGO core@shell nanocubes exhibit a lattice spacing of about 0.27 nm conforming to (104) plane of α-Fe_2O_3 nanocubes. Fig. 2e and j displaying a selected area electron diffraction (SAED) patterns of the α-Fe_2O_3@rGO core@shell nanocubes, indicating a ring pattern with dots. It further confirms the polycrystalline nature of α-Fe_2O_3 present in the α-Fe_2O_3@rGO core@shell nanocubes. The diffractions of (012), (104), (110), (113), (024), and (116) planes confirm the presence of α-Fe_2O_3 in the α-Fe_2O_3@rGO core@shell nanocubes.

The elemental composition of the α-Fe_2O_3@rGO core@shell nanocubes was studied using FE-SEM EDS and TEM-EDS analysis. The FE-SEM EDS images are shown in Figs. S5 and S6 and TEM-EDS images are shown in Fig. 2(k-p) and 2(q-v) corresponding to α-Fe_2O_3@rGO-10 wt% and α-Fe_2O_3@rGO-20 wt% samples, respectively. The TEM-EDS color mapping analysis clearly shows iron and oxygen in the core regime and carbon in the shell region. Moreover, the color maps of carbon indicating complete wrapping of rGO sheets over the surface of α-Fe_2O_3 nanocubes further confirm the formation of α-Fe_2O_3@rGO core@shell nanocubes. TEM-EDS spectra also verify the presence of iron, oxygen, and carbon in these samples. Later, the elemental composition and surface electronic states of the rGO, α-Fe_2O_3, and α-Fe_2O_3@rGO core@shell nanocubes were examined using XPS analysis. The survey spectra of pure α-Fe_2O_3 and rGO are shown in Figs. S7a and S7d. In the pure α-Fe_2O_3, the high-resolution XPS spectrum of Fe2p (Fig. S7b) illustrations two peaks centered at 710.5 and 724.2 eV, agreeing to $Fe2p_{3/2}$ and $Fe2p_{1/2}$, respectively, along with two other satellite peaks [34,35]. The $Fe2p_{3/2}$ and $Fe2p_{1/2}$ show two doublets at 710.3 & 723.6 eV, and 711.9 & 725.5 eV indicating +2 and + 3 oxidation states of iron present in the α-Fe_2O_3 [34]. The high-resolution spectrum of O1s (Fig. S7c) shows peaks at 529.9, 531.9, and 534.7 eV, conforming to O–Fe, –OH, and –OH_2, respectively, indicating the presence of hydroxyl groups on the surface of α-Fe_2O_3 [36]. In the case of rGO, the high-resolution spectrum of C1s (Fig. S7e) shows three peaks centered at 284.5 (C═C), 285.7 (C–O), and 288.5 eV (O–C═O), respectively [26]. Fig. 3a and **S8a** indicate the survey spectra of the α-Fe_2O_3@rGO core@shell nanocubes, confirming the presence of iron, oxygen, and carbon in these samples. The high-resolution XPS spectra of Fe2p (Figs. 3b and S8b) show similar features like Fe2p of pure α-Fe_2O_3. The high-resolution spectra of O1s are displayed in Figs. 3c and S8c display three peaks positioned at about 529.8 eV corresponding to O–Fe bond in the α-Fe_2O_3, and other two peaks at 531.5 and 533.2 eV consistent to O═C and C–OH/O–C–O of rGO, respectively [13,35,37], representing the strong bonding between the α-Fe_2O_3 and rGO in the α-Fe_2O_3@rGO core@shell samples. Figs. 3d and S8d display the high-resolution spectra of C1s, which show the peaks similar to C1s of rGO. These results further supporting the formation of α-Fe_2O_3@rGO core@shell samples.

It is known that rGO can play a significant role in enlightening the rate capability and cyclic stability of the active electrode materials.

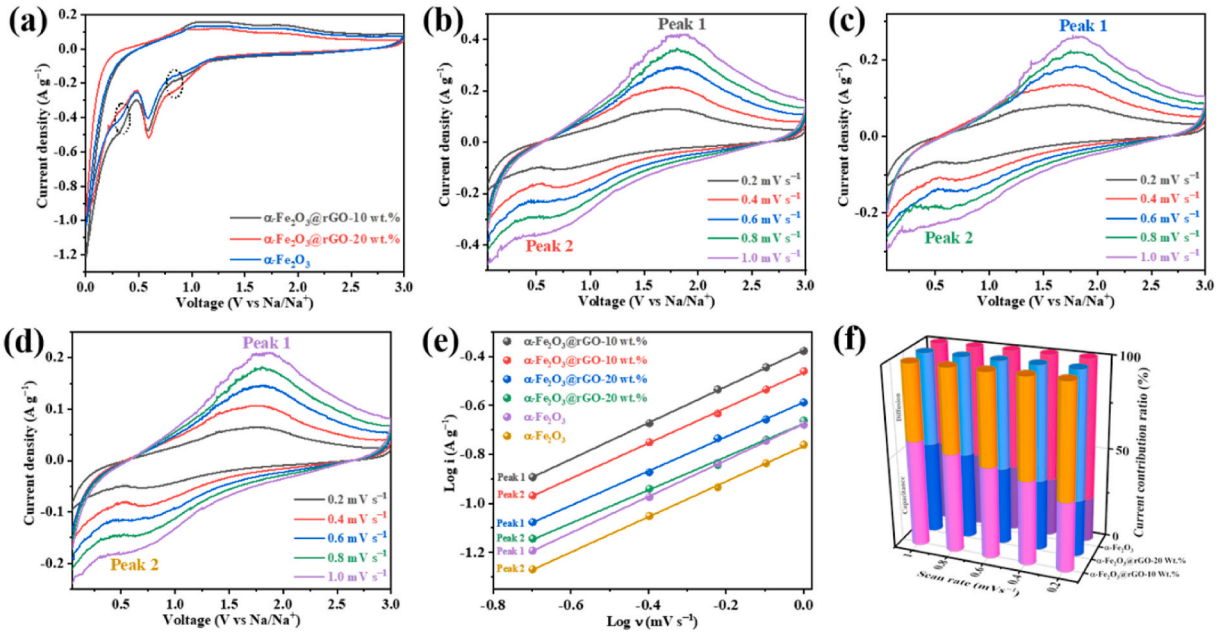

Fig. 4. (a) CV spectra of α-Fe_2O_3 and α-Fe_2O_3@rGO core@shell nanocubes in a first cycle at a scan rate of 0.2 mV s^{-1}, (b–d) CV spectra of α-Fe_2O_3@rGO-10 wt%, α-Fe_2O_3@rGO-20 wt%, and α-Fe_2O_3 at scan rates between 0.2 and 1.0 mV s^{-1}, respectively, (e) Log i *vs.* Log *ν* plot, and (f) 3D plot of capacitive and diffusion current contribution ratio of α-Fe_2O_3 and α-Fe_2O_3@rGO core@shell nanocubes.

Electrochemical studies (cyclic voltammetry (CV), Galvanostatic charge-discharge (GCD), rate capability, and cyclic stability) were performed in a half-cell system to empathize the Na-ion charge storage in α-Fe_2O_3@rGO core@shell nanocubes. Fig. 4a displays the CV plot of α-Fe_2O_3 and α-Fe_2O_3@rGO core@shell nanocube samples in the first cycle at a scan rate of 0.2 mV s^{-1}. All three samples show two weak (0.85 & 0.33 V *vs.* Na/Na^+) and two strong (0.61 & 0.01 V *vs.* Na/Na^+) reduction peaks and two oxidation peaks at 0.87/1.00 and 1.92 V *vs.* Na/Na^+. A weak reduction peak at 0.85 V *vs.* Na/Na^+ is credited to Na-ion insertion into the lattice of α-Fe_2O_3 leads to α-$Na_xFe_2O_3$ [13]. A strong reduction peak at 0.61 V *vs.* Na/Na^+ is caused by forming a solid electrolyte interface (SEI) accompanied by the electrolyte decomposition leading to an irreversible capacity loss in the first cycle [13,22]. Another weak and strong reduction peaks at 0.33 and 0.01 V *vs.* Na/Na^+ are ascribed to the reduction of the α-Fe_2O_3 from Fe^{3+}→Fe^{2+} and Fe^{2+}→Fe^0, respectively [23,24]. The α-Fe_2O_3 and α-Fe_2O_3@rGO-10 wt% samples show the oxidation peaks at about 1.00 and 1.92 V *vs.* Na/Na^+ and that of α-Fe_2O_3@rGO-20 wt% shows at about 0.87 and 1.92 V *vs.* Na/Na^+ corresponding to Fe^0→Fe^{2+} and Fe^{2+}→Fe^{3+}, correspondingly [23,24]. The whole electrochemical process is expressed as follows [38–41].

$$Fe_2O_3 + 6Na^+ + 6e^- \rightarrow 3Na_2O + 2Fe \quad (2)$$

The CV analysis of α-Fe_2O_3 and α-Fe_2O_3@rGO core@shell nanocubes were tested at diverse scan rates from 0.2 to 1.0 mV s^{-1} to understand the kinetics of the electrodes (Fig. 4b–d). All three samples show a broad reduction peak between 1.15 and 0.50 V *vs.* Na/Na^+ with a peak centered at about 0.72 V *vs.* Na/Na^+ corresponding to Fe^{3+}→Fe^0 [23]. The broad oxidation peak is noticed between 1.20 and 2.25 V *vs.* Na/Na^+ with a peak centered at about 1.75 V *vs.* Na/Na^+ corresponding to Fe^0→Fe^{3+} [40,41]. Moreover, with proliferating the scan rate, redox peaks are shifted towards lower and higher potential sides without altering the shape of the peaks indicating the excellent reversibility of the redox reactions [2,42]. Among the three electrodes, the α-Fe_2O_3@rGO-10 wt% sample shows higher current with the increase of scan rate, indicating better electrochemical performance than other samples. To understand the charge storage mechanism, peak current (i_p) at various scan rates was evaluated using the following equations [31,42].

$$i = a\nu^b \quad (3)$$

$$\log i = \log a + b\log \nu \quad (4)$$

Fig. 4e shows a linear association between log i and log *ν* with a slope (b) values greater than 0.5, indicating the significant charge storage contribution is because of capacitive behavior (b = 1.0) rather than ion-diffusion controlled process (b = 0.5) in these samples [43,44]. The slope values for peak 1 are 0.69, 0.74, and 0.70, and that of peak 2 are 0.66, 0.72, and 0.68, corresponding to α-Fe_2O_3, α-Fe_2O_3@rGO-10 wt% and α-Fe_2O_3@rGO-20 wt% samples, respectively. The following equation is employed to enumerate capacitive ($k_1\nu$) contribution and ion-diffusion controlled ($k_2\nu^{1/2}$) process in these samples.

$$i(V) = k_1\nu + k_2\nu^{1/2} \quad (5)$$

The contribution of charge storage of α-Fe_2O_3, α-Fe_2O_3@rGO-10 wt %, and α-Fe_2O_3@rGO-20 wt% samples at different scan rates is shown in Fig. 4f. It is noticed that with the rise of scan rate from 0.2 to 1.0 mV s^{-1}, the capacitive impact is gradually increased, and the ion-diffusion contribution is decreased for all three samples. Among the three samples, the α-Fe_2O_3@rGO-10 wt% sample shows a higher capacitive contribution than the rest of the samples. The better electrochemical performance of the α-Fe_2O_3@rGO-10 wt% sample is mainly ascribed to synergistic interaction of porous α-Fe_2O_3 with an interconnected network of rGO layers, which can decrease the diffusion path length for Na-ion shuttling and enhances the electrochemical activity [12,22].

To empathize the electrochemical performance of the α-Fe_2O_3 and α-Fe_2O_3@rGO core@shell nanocubes, GCD analysis was accomplished at various C-rates ranging from 0.1 to 5.0C (1.0C = 1000 mA g^{-1}), and the corresponding results are shown in Fig. 5a–c. The first discharge and charge capacities for α-Fe_2O_3@rGO-10 wt% sample are found to be 1661.6 and 920.8 mAh g^{-1} with a CE of 55.5%, and that of α-Fe_2O_3 and α-Fe_2O_3@rGO-20 wt% samples are found to be 1500.7 & 904.8 mAh g^{-1} and 942.0 & 476.1 mAh g^{-1} with a CEs of 60.3% and 50.5%, respectively. The discharge capacities in the second cycle are measured to be about 970.2, 505.3, and 910.3 mAh g^{-1} corresponding to α-Fe_2O_3@rGO-10 wt%, α-Fe_2O_3@rGO-20 wt%, and α-Fe_2O_3, respectively. The low CE in the first cycle and irreversible capacity loss between the first and

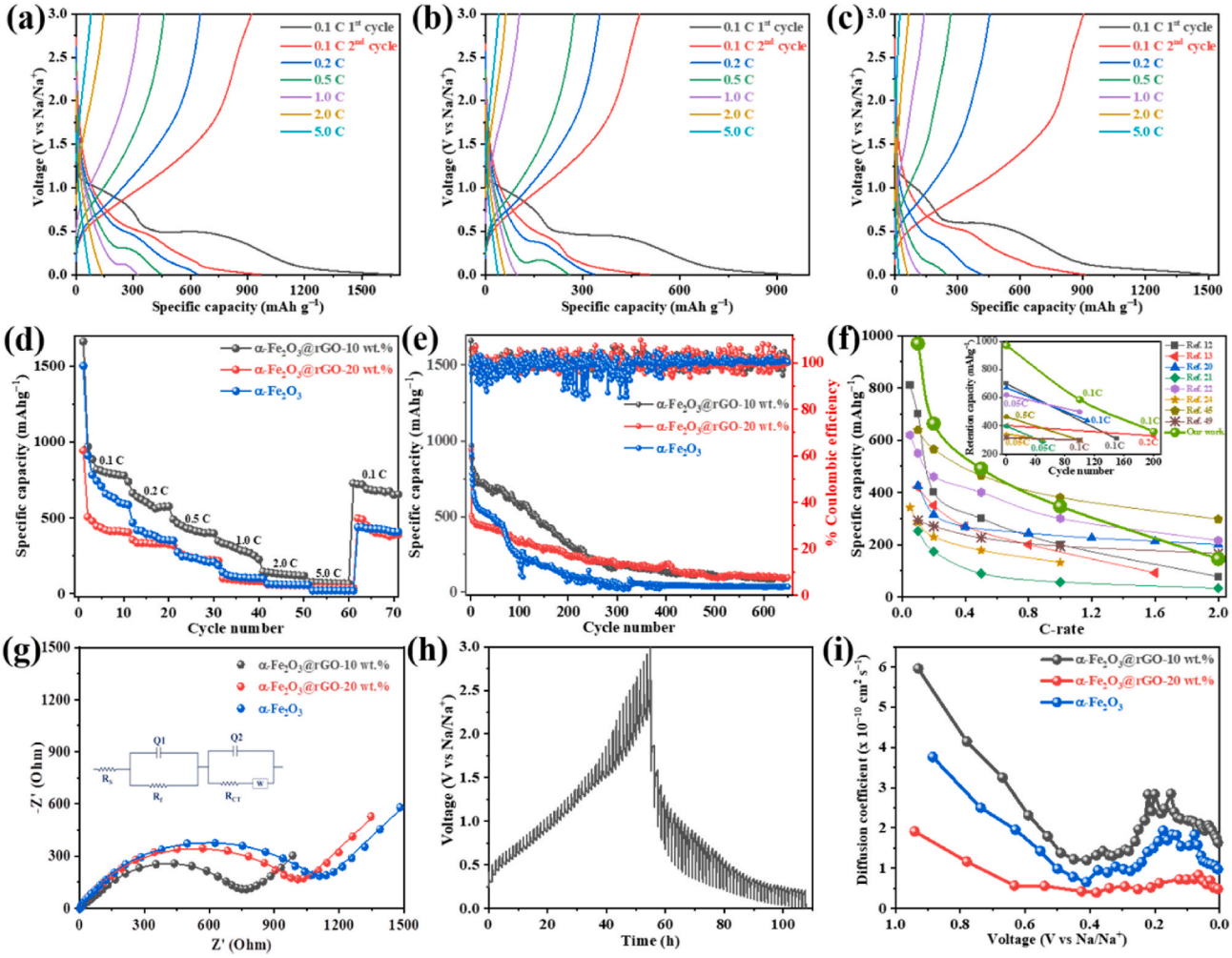

Fig. 5. (a–c) GCD plots of α-Fe_2O_3@rGO-10 wt%, α-Fe_2O_3@rGO-20 wt%, and α-Fe_2O_3 at various C-rates, respectively, (d) rate capability, (e) cyclic stability at 0.1 C-rate, (f) comparison of specific capacity and rate capability of α-Fe_2O_3@rGO-10 wt% sample with a reported Fe_2O_3/rGO materials (inset shows the comparison of retention capacity after cyclic stability), (g) EIS spectra at 650th cycle of α-Fe_2O_3 and α-Fe_2O_3@rGO core@shell nanocubes (corresponding lines are indicating fitting curves); inset shows the corresponding equivalent circuit, (h) GITT plot of α-Fe_2O_3@rGO-10 wt% sample at 0.1 C-rate, and (i) chemical diffusion coefficient of Na-ion as a function of voltage during the discharge curves of GITT in the α-Fe_2O_3 and α-Fe_2O_3@rGO samples.

second cycle is commonly observed for conversion-based metal oxide nanoparticles. It is primarily accredited to establishing the SEI layer by decomposing the electrolyte, indicating a reduction peak at about 0.61 V *vs.* Na/Na^+ and irreversible intercalation of Na-ions into the crystal lattice of α-Fe_2O_3 in the first cycle [38,39]. Among the three samples, the α-Fe_2O_3@rGO-10 wt% sample shows higher discharge capacity in the second cycle. We were fabricated the α-Fe_2O_3@rGO freestanding electrodes along with SWCNTs. To understand SWCNTs' specific capacity contribution in these electrodes, we were carried out GCD analysis with SWCNTs electrode alone with an electrode mass of 1.0 mg cm^{-2} (Fig. S9). It exhibits a specific capacity of about 100 mAh g^{-1} at 0.1C. In the case of α-Fe_2O_3@rGO freestanding electrodes, the mass of SWCNTs is about 0.2 mg cm^{-2}, and the contribution of SWCNTs' can be about five times lower when compared with an SWCNTs mass of 1.0 mg cm^{-2}, corresponding to a specific capacity contribution of about 20 mAh g^{-1} at 0.1C. The α-Fe_2O_3@rGO-10 wt% freestanding electrode shows a specific capacity of 970.2 mAh g^{-1}; the contribution of SWCNTs' in this electrode is about 2.0% of its overall capacity, and the significant contribution (98.0%) is shown by α-Fe_2O_3@rGO alone. Afterward, the rate capability of all the three samples was tested, and the corresponding plot is shown in Fig. 5d. The discharge capacities of α-Fe_2O_3@rGO-10 wt% sample are found to be 663.2, 490.9, 346.7, 145.4, and 77.8 mAh g^{-1} at a C-rates of 0.2, 0.5, 1.0, 2.0 and 5.0C, correspondingly, and that of α-Fe_2O_3@rGO-20 wt%, and α-Fe_2O_3 are estimated to be 355.7, 276.5, 101.7, 60.7, & 39.5 mAh g^{-1}, and 467.9, 273.5, 142.0, 65.4, & 20.3 mAh g^{-1} at a same C-rates, respectively. The slight decay in specific capacities at low C-rate is primarily accredited to the continuous formation of stable SEI accompanied by side reactions of the electrolyte [12,24]. When the C-rate brings back to 0.1C, the α-Fe_2O_3@rGO electrodes show better discharge capacities than α-Fe_2O_3 electrode indicating better rate capability. Among the α-Fe_2O_3@rGO core@shell samples, the α-Fe_2O_3@rGO-20 wt% sample may possess low electrical conductivity because excess rGO might have blocked the active sites for Na-ion diffusion in α-Fe_2O_3 and thus resulting in a low specific capacity as well as rate capability at all C-rates than that of α-Fe_2O_3@rGO-10 wt% sample.

The cyclic stability of all the three samples until 650 cycles at 0.1 C-rate is displayed in Fig. 5e. After 100 cycles, the α-Fe_2O_3@rGO-10 wt% sample displays a discharge capacity of 586.9 mAh g^{-1}, while α-Fe_2O_3@rGO-20 wt% and α-Fe_2O_3 samples show 340.9 and 242.7 mAh g^{-1}. In the case of α-Fe_2O_3 nanocubes, the discharge capacity is fallen rapidly after 65 cycles and showed much fluctuation in the CE, which can be due to the faster aggregation of α-Fe_2O_3 nanocubes by the large volume changes during the cycling [12,20,39]. From the 101th to 300th cycle, discharge capacities are slowly decayed, and afterward, prolonged decay is observed until the 650th cycle in the α-Fe_2O_3@rGO

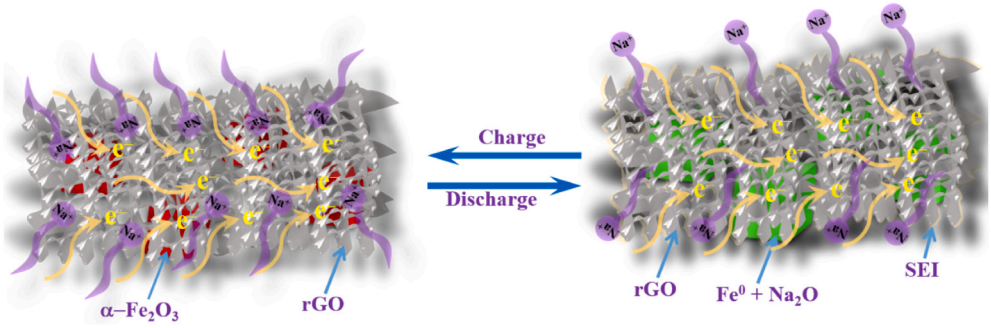

Fig. 6. A schematic illustration of Na-ion storage during the charge and discharge in the α-Fe_2O_3@rGO core@shell nanocubes.

core@shell samples. At the 650th cycle, discharge capacities are 98.2, 98.7, and 37.2 mAh g^{-1} corresponding to α-Fe_2O_3@rGO-10 wt%, α-Fe_2O_3@rGO-20 wt%, and α-Fe_2O_3, respectively. The α-Fe_2O_3@rGO samples show about two and half times higher discharge capacities after 650 cycles than pure α-Fe_2O_3 alone. The better discharge capacity of α-Fe_2O_3@rGO core@shell nanocubes is mainly attributed to slowing the aggregation of α-Fe_2O_3 by the interconnected rGO network and shortening the path length for Na-ion shuttling during the cycling [13,39]. The comparison of specific capacity, rate capability, and cyclic stability of α-Fe_2O_3@rGO core@shell nanocubes with previously reported literature were summarized in Table S1 [12,13,19–24,45–49] and also provided in Fig. 5f. As compared to previously reported α-Fe_2O_3/rGO electrode materials, the α-Fe_2O_3@rGO core@shell nanocubes exhibit superior initial specific capacity and cyclic stability.

Afterward, the electrode kinetics of the samples were tested at the 650th cycle using EIS, and the corresponding results are shown in Fig. 5g. All the parameters were evaluated by fitting the curve according to the equivalent circuit model [13,23]. In the high-frequency region, solution resistance (R_s) of α-Fe_2O_3@rGO-10 wt%, α-Fe_2O_3@rGO-20 wt%, and α-Fe_2O_3 is found to be 2.63, 2.76, and 3.03 Ω, respectively. The SEI film resistance (R_f) is measured to be 91, 207, and 242 Ω corresponding to α-Fe_2O_3@rGO-10 wt%, α-Fe_2O_3@rGO-20 wt%, and α-Fe_2O_3, respectively. The lower R_f value of α-Fe_2O_3@rGO-10 wt% indicates lesser electrolyte decomposition to form the SEI layer on the surface of α-Fe_2O_3@rGO-10 wt% than that of α-Fe_2O_3@rGO-20 wt%, and α-Fe_2O_3 [23]. The depressed semicircle is a parallel coalescence of charge transfer resistance (R_{ct}) and constant phase element (Q). The R_{ct} is calculated to be 750, 1001, and 1106 Ω corresponding to α-Fe_2O_3@rGO-10 wt%, α-Fe_2O_3@rGO-20 wt%, and α-Fe_2O_3, respectively, indicating the α-Fe_2O_3@rGO-10 wt% possesses faster electron transfer than α-Fe_2O_3@rGO-20 wt%, and α-Fe_2O_3 because of its better electrical conductivity [12]. In the low-frequency region, the inclined line exhibited a similar slope for all the samples indicating similar diffusion. EIS results indicating better electrode kinetics in α-Fe_2O_3@rGO samples than α-Fe_2O_3 because of better electrical conductivity offered by rGO in these samples. To study the Na-ion diffusion coefficient in these samples, we were performed the GITT analysis, and the corresponding GITT plot of the α-Fe_2O_3@rGO-10 wt% sample is shown in Fig. 5h and that of α-Fe_2O_3 and α-Fe_2O_3@rGO-20 wt% samples are shown in Fig. S10a &b. The single titration of the α-Fe_2O_3@rGO-10 wt% sample during the discharge is shown in Fig. S10c. During the second charge-discharge cycle, the Na-ion diffusion coefficient was estimated according to Fick's second law [50].

$$D_{Na} = \frac{4}{\pi\tau}\left(m_B V_M / M_w A\right)^2 \left(\Delta E_s / \Delta E_\tau\right)^2 \quad (6)$$

Here, D is the Na-ion diffusion coefficient ($cm^2\ s^{-1}$), τ is the pulse time of single titration (s), m_B is the mass of active material (g), V_M is the molar volume of the active material ($cm^3\ mol^{-1}$), M_w is the molecular weight of the active material ($g\ mol^{-1}$), A is the active surface area at the electrode-electrolyte interface (cm^2), ΔE_s is the steady-state potential, and ΔE_τ is the total difference in the cell voltage during the single titration. The chemical Na-ion diffusion coefficient as a function of voltage is showing in Fig. 5i, which reveals that α-Fe_2O_3@rGO-10 wt% sample shows Na-ion diffusion coefficient 5.96×10^{-10} to 1.93×10^{-10} $cm^2\ s^{-1}$, while that of α-Fe_2O_3@rGO-20 wt% and α-Fe_2O_3 samples show 1.91×10^{-10} to 4.84×10^{-11} $cm^2\ s^{-1}$ and 3.76×10^{-10} to 9.74×10^{-11} $cm^2\ s^{-1}$, respectively. Among the three samples, the α-Fe_2O_3@rGO-10 wt% sample shows a higher Na-ion diffusion coefficient indicating better Na-ion diffusion favored by rGO layers over the surface of α-Fe_2O_3, whereas low Na-ion diffusion coefficient in the α-Fe_2O_3@rGO-20 wt% sample indicating blockage of surface pores of α-Fe_2O_3 by excess rGO. These results further support the better specific capacity and rate capability of the α-Fe_2O_3@rGO-10 wt% sample.

Finally, the morphology of the α-Fe_2O_3@rGO samples was tested using FE-SEM analysis after the cyclic stability test, and the corresponding results are shown in Fig. S11. Both the α-Fe_2O_3@rGO samples show a slight aggregation of α-Fe_2O_3 nanocubes after 650 cycles. These samples show SWCNTs in the FE-SEM images because these freestanding electrodes were fabricated with the help of SWCNTs. Based on the above results, a schematic illustration of Na-ion storage in the α-Fe_2O_3@rGO samples during the charge-discharge cycles is depicted in Fig. 6. The better activity and high structural stability of α-Fe_2O_3@rGO core@shell nanocubes is mainly attributing to the efficient synergistic interaction between the α-Fe_2O_3 nanocubes and rGO layers [21,24]. Moreover, the porous structure of α-Fe_2O_3 nanocubes can prevent significant volume changes during the cyclic stability; the rGO network can provide better conductivity to improve the activity and structural integrity of the α-Fe_2O_3@rGO core@shell nanocubes [12]. Therefore, tuning the porous structure of active materials with a 3D morphology and coupling with them by an rGO network can enormously improve the electrochemical activity of the functional materials. Because of these reasons, α-Fe_2O_3@rGO, core@shell nanocubes show excellent electrochemical properties than α-Fe_2O_3 nanocubes alone. These insights can be helpful to develop various electroactive materials in the future for energy storage applications.

3. Conclusion

We have effectively demonstrated the gram-scale synthesis of α-Fe_2O_3@rGO core@shell nanocubes via a direct and economical solution route. The synthesized α-Fe_2O_3@rGO core@shell nanocubes samples were well characterized to confirm the phase purity, surface oxidation states, and morphology by various analytical techniques. The synthesized α-Fe_2O_3@rGO core@shell nanocubes were deliberated as effective anode materials for SIBs. The α-Fe_2O_3@rGO-10 wt% sample shows a specific capacity of about 970.2 mAh g^{-1} at 0.1 C-rate. Moreover, it also delivers an excellent rate capability of about 77.8 mAh g^{-1} at 5.0 C-rate. In addition, the α-Fe_2O_3@rGO-10 wt% sample also displays a specific capacity of approximately 586.9 mAh g^{-1} after 100 cycles at 0.1 C-rate. The better specific capacity, rate capability, and cyclic stability mainly contribute to the synergistic interaction between

porous α-Fe_2O_3 and rGO. The current synthetic strategy expects to reduce the cost of synthesizing various electroactive materials in the future and will help design effective anode materials for different practical energy storage devices.

Author statement

Syam Kandula: Investigation, Writing - Original Draft, **Junho Bae**: Methodology. **Jinhan Cho**: Supervision, **Jeong Gon Son**: Writing-Reviewing and Editing, Supervision.

Declaration of competing interest

The authors declare that they have no known competing financial interests or personal relationships that could have appeared to influence the work reported in this paper.

Acknowledgment

This work was mainly supported by Brain Pool Program through the National Research Foundation of Korea (NRF), funded by the Ministry of Science and ICT (Grant no.2019H1D3A1A01070498). We also gratefully acknowledge financial support from the Korea Institute of Science and Technology (KIST) institutional and KU-KIST programs (Project No. 2E31161) and the National Research Foundation of Korea (NRF) grant funded by the Korea government (MEST) (No. NRF-2019R1A2C2005657).

Appendix A. Supplementary data

Supplementary data to this article can be found online at https://doi.org/10.1016/j.compositesb.2021.108995.

References

[1] Liu T, Zhang L, Cheng B, Yu J. Hollow carbon spheres and their hybrid nanomaterials in electrochemical energy storage. Adv Energy Mater 2019;9:1803900. https://doi.org/10.1002/aenm.201803900.
[2] Kandula S, Shrestha KR, Kim NH, Lee JH. Fabrication of a 3D hierarchical sandwich Co_9S_8/α-MnS@N–C@MoS_2 nanowire architectures as advanced electrode material for high performance hybrid supercapacitors. Small 2018;14:1800291. https://doi.org/10.1002/smll.201800291.
[3] Liu Y, Li X, Shen W, Dai Y, Kou W, Zheng W, et al. Multishelled transition metal-based microspheres: synthesis and applications for batteries and supercapacitors. Small 2019;15:1804737. https://doi.org/10.1002/smll.201804737.
[4] Kandula S, Shrestha KR, Rajeshkhanna G, Kim NH, Lee JH. Kirkendall growth and ostwald ripening induced hierarchical morphology of Ni-Co LDH/$MMoS_x$ (M = Co, Ni, and Zn) heteronanostructures as advanced electrode materials for asymmetric solid-state supercapacitors. ACS Appl Mater Interfaces 2019;11:11555–67. https://doi.org/10.1021/acsami.9b02978.
[5] Kang S, Hong SY, Kim N, Oh J, Park M, Chung KY, et al. Stretchable lithium-ion battery based on Re-entrant micro-honeycomb electrodes and cross-linked gel electrolyte. ACS Nano 2020;14:3660–8. https://doi.org/10.1021/acsnano.0c00187.
[6] Kim E, Kim H, Park B-J, Han Y-H, Park JH, Cho J, et al. Etching-Assisted crumpled graphene wrapped spiky iron oxide particles for high-performance Li-ion hybrid supercapacitor. Small 2018;14:1704209. https://doi.org/10.1002/smll.201704209.
[7] Qi S, Xu B, Tiong VT, Hu J, Ma J. Progress on iron oxides and chalcogenides as anodes for sodium-ion batteries. Chem Eng J 2020;379:122261. https://doi.org/10.1016/j.cej.2019.122261.
[8] Jagadale A, Zhou X, Xiong R, Dubal DP, Xu J, Yang S. Lithium ion capacitors (LICs): development of the materials. Energy Storage Mater 2019;19:314–29. https://doi.org/10.1016/j.ensm.2019.02.031.
[9] Ding J, Hu W, Paek E, Mitlin D. Review of hybrid ion capacitors: from aqueous to lithium to sodium. Chem Rev 2018;118:6457–98. https://doi.org/10.1021/acs.chemrev.8b00116.
[10] Wang H, Zhu C, Chao D, Yan Q, Fan HJ. Nonaqueous hybrid lithium-ion and sodium-ion capacitors. Adv Mater 2017;29:1702093. https://doi.org/10.1002/adma.201702093.
[11] Li F, Zhou Z. Micro/nanostructured materials for sodium ion batteries and capacitors. Small 2018;14:1702961. https://doi.org/10.1002/smll.201702961.
[12] Zhang ZJ, Wang YX, Chou SL, Li HJ, Liu HK, Wang JZ. Rapid synthesis of α-Fe_2O_3/rGO nanocomposites by microwave autoclave as superior anodes for sodium-ion batteries. J Power Sources 2015;280:107–13. https://doi.org/10.1016/j.jpowsour.2015.01.092.
[13] Kong D, Cheng C, Wang Y, Liu B, Huang Z, Yang HY. Seed-assisted growth of α-Fe_2O_3 nanorod arrays on reduced graphene oxide: a superior anode for high-performance Li-ion and Na-ion batteries. J Mater Chem A 2016;4:11800–11. https://doi.org/10.1039/C6TA04370D.
[14] Zhang H, Hu M, Lv Q, Huang Z, Kang F, Lv R. Advanced materials for sodium-ion capacitors with superior energy–power properties: progress and perspectives. Small 2020;16:1902843. https://doi.org/10.1002/smll.201902843.
[15] Kim J, Choi MS, Shin KH, Kota M, Kang Y, Lee S, et al. Rational design of carbon nanomaterials for electrochemical sodium storage and capture. Adv Mater 2019;31:1803444. https://doi.org/10.1002/adma.201803444.
[16] Yun S, Bak S, Kim S, Yeon JS, Kim MG, Yang X, et al. Rational design of hierarchically open-porous spherical hybrid architectures for lithium-ion batteries. Adv Energy Mater 2019;9:1802816. https://doi.org/10.1002/aenm.201802816.
[17] Shin KH, Park SK, Nakhanivej P, Wang Y, Liu P, Bak SM, et al. Biomimetic composite architecture achieves ultrahigh rate capability and cycling life of sodium ion battery cathodes. Appl Phys Rev 2020;7:041410. https://doi.org/10.1063/5.0020805.
[18] Zhang Y, Jiang J, An Y, Wu L, Dou H, Zhang J, et al. Sodium-ion capacitors: materials, mechanism, and challenges. ChemSusChem 2020;13:2522–39. https://doi.org/10.1002/cssc.201903440.
[19] Wu X, Chen W, Key J, Wu W. One-pot solvothermal synthesis of fern leaf-like α-Fe_2O_3@C/graphene from ferrocene with enhanced lithium and sodium storage properties. Powder Technol 2018;323:424–32. https://doi.org/10.1016/j.powtec.2017.10.028.
[20] Wang S, Zhu Y, Sun X, Liu H, Cui J, Zhang Y, et al. N, S co-doped modified graphene/Fe_2O_3 composites synthesized via microwave-assisted method for Na-ion batteries. Inorg Chem Commun 2020;121:108188. https://doi.org/10.1016/j.inoche.2020.108188.
[21] Liu X, Chen T, Chu H, Niu L, Sun Z, Pan L, et al. Fe_2O_3-Reduced graphene oxide composites synthesized via microwave-assisted method for sodium ion batteries. Electrochim Acta 2015;166:12–6. https://doi.org/10.1016/j.electacta.2015.03.081.
[22] Li T, Qin A, Yang L, Chen J, Wang Q, Zhang D, et al. In situ grown Fe_2O_3 single crystallites on reduced graphene oxide nanosheets as high performance conversion anode for sodium-ion batteries. ACS Appl Mater Interfaces 2017;9:19900–7. https://doi.org/10.1021/acsami.7b04407.
[23] Li D, Zhou J, Chen X, Song H. Amorphous Fe_2O_3/graphene composite nanosheets with enhanced electrochemical performance for sodium-ion battery. ACS Appl Mater Interfaces 2016;8:30899–907. https://doi.org/10.1021/acsami.6b09444.
[24] Meng S, Zhao D-L, Wu L-L, Ding Z-W, Cheng X-W, Hu T. Fe_2O_3/Nitrogen-doped graphene nanosheet nanocomposites as anode materials for sodium-ion batteries with enhanced electrochemical performance. J Alloys Compd 2018;737:130–5. https://doi.org/10.1016/j.jallcom.2017.12.077.
[25] Shrestha KR, Kandula S, Kim NH, Lee JH. Core cation tuned $M_xCo_{3-x}S_4$@$NiMoS_4$ [M = Ni, Mn, Zn] core-shell nanomaterials as advanced all solid-state asymmetric supercapacitor electrodes. Chem Eng J 2021;405:127046. https://doi.org/10.1016/j.cej.2020.127046.
[26] Shrestha KR, Kandula S, Kim NH, Lee JH. A spinel $MnCo_2O_4$/NG 2D/2D hybrid nanoarchitectures as advanced electrode material for high performance hybrid supercapacitors. J Alloys Compd 2019;771:810–20. https://doi.org/10.1016/j.jallcom.2018.09.032.
[27] Sugimoto T, Sakata K. Preparation of monodisperse pseudocubic α-Fe_2O_3 particles from condensed ferric hydroxide gel. J Colloid Interface Sci 1992;152:587–90. https://doi.org/10.1016/0021-9797(92)90062-Q.
[28] Bersani D, Lottici PP, Montenero A. Micro-Raman investigation of iron oxide films and powders produced by sol-gel syntheses. J Raman Spectrosc 1999;30:355–60. https://doi.org/10.1002/(SICI)1097-4555(199905)30:5<355::AID-JRS398>3.0.CO;2-C.
[29] de Faria DLA, Lopes FN. Heated goethite and natural hematite: can Raman spectroscopy be used to differentiate them? Vib Spectrosc 2007;45:117–21. https://doi.org/10.1016/j.vibspec.2007.07.003.
[30] Martin TP, Merlin R, Huffman DR, Cardona M. Resonant two magnon Raman scattering in α-Fe_2O_3. Solid State Commun 1977;22:565–7. https://doi.org/10.1016/0038-1098(77)90137-5.
[31] Jing P, Wang Q, Wang B, Gao X, Zhang Y, Wu H. Encapsulating yolk-shell FeS_2@carbon microboxes into interconnected graphene framework for ultrafast lithium/sodium storage. Carbon 2020;159:366–77. https://doi.org/10.1016/j.carbon.2019.12.060.
[32] Wang X, Chen K, Wang G, Liu X, Wang H. Rational design of three-dimensional graphene encapsulated with hollow FeP@carbon nanocomposite as outstanding anode material for lithium ion and sodium ion batteries. ACS Nano 2017;11:11602–16. https://doi.org/10.1021/acsnano.7b06625.
[33] Prabakar SJR, Jeong J, Pyo M. Highly crystalline prussian blue/graphene composites for high-rate performance cathodes in Na-ion batteries. RSC Adv 2015;5:37545–52. https://doi.org/10.1039/C5RA04769B.
[34] Zhan J, Wu K, Yu X, Yang M, Cao X, Lei B, et al. α-Fe_2O_3 nanoparticles decorated C@MoS_2 nanosheet arrays with expanded spacing of (002) plane for ultrafast and high Li/Na-ion storage. Small 2019;15:1901083. https://doi.org/10.1002/smll.201901083.
[35] Wang L, Yang H, Liu X, Zeng R, Li M, Huang Y, et al. Constructing hierarchical tectorum-like α-Fe_2O_3/PPy nanoarrays on carbon cloth for solid-state asymmetric supercapacitors. Angew Chem Int Ed 2017;56:1105–10. https://doi.org/10.1002/anie.201609527.

[36] Wang JC, Ren J, Yao HC, Zhang L, Wang JS, Zang SQ, et al. Synergistic photocatalysis of Cr(VI) reduction and 4-chlorophenol degradation over hydroxylated α-Fe_2O_3 under visible light irradiation. J Hazard Mater 2016;311:11–9. https://doi.org/10.1016/j.jhazmat.2016.02.055.

[37] Luo Y, Luo J, Jiang J, Zhou W, Yang H, Qi X, et al. Seed-assisted synthesis of highly ordered TiO_2@α-Fe_2O_3 core/shell arrays on carbon textiles for lithium-ion battery applications. Energy Environ Sci 2012;5:6559. https://doi.org/10.1039/c2ee03396h.

[38] Zhang N, Han X, Liu Y, Hu X, Zhao Q, Chen J. 3D porous γ-Fe_2O_3@C nanocomposite as high-performance anode material of Na-ion batteries. Adv Energy Mater 2015;5:1401123. https://doi.org/10.1002/aenm.201401123.

[39] Jian Z, Zhao B, Liu P, Li F, Zheng M, Chen M, et al. Fe_2O_3 nanocrystals anchored onto graphene nanosheets as the anode material for low-cost sodium-ion batteries. Chem Commun 2014;50:1215–7. https://doi.org/10.1039/C3CC47977C.

[40] Philippe B, Valvo M, Lindgren F, Rensmo H, Edström K. Investigation of the electrode/electrolyte interface of Fe_2O_3 composite electrodes: Li vs Na batteries. Chem Mater 2014;26:5028–41. https://doi.org/10.1021/cm5021367.

[41] Shi L, Li Y, Zeng F, Ran S, Dong C, Leu S-Y, et al. In situ growth of amorphous Fe_2O_3 on 3D interconnected nitrogen-doped carbon nanofibers as high-performance anode materials for sodium-ion batteries. Chem Eng J 2019;356:107–16. https://doi.org/10.1016/j.cej.2018.09.018.

[42] Shrestha KR, Kandula S, Rajeshkhanna G, Srivastava M, Kim NH, Lee JH. An advanced sandwich-type Architecture of $MnCo_2O_4$@N-C@MnO_2 as an efficient electrode material for a high-energy density hybrid asymmetric solid-state supercapacitor. J Mater Chem A 2018;6:24509–22. https://doi.org/10.1039/c8ta08976k.

[43] Zang R, Li P, Guo X, Man Z, Zhang S, Wang C, et al. Yolk–shell N-doped carbon coated FeS_2 nanocages as a high-performance anode for sodium-ion batteries. J Mater Chem A 2019;7:14051–9. https://doi.org/10.1039/C9TA03917A.

[44] Wang F, Zhang W, Zhou H, Chen H, Huang Z, Yan Z, et al. Preparation of porous FeS_2-C/RG composite for sodium ion batteries. Chem Eng J 2020;380:122549. https://doi.org/10.1016/j.cej.2019.122549.

[45] Chen Y, Guo Z, Jian B, Zheng C, Zhang H. N-doped modified graphene/Fe_2O_3 nanocomposites as high-performance anode material for sodium ion storage. Nanomaterials 2019;9:1770. https://doi.org/10.3390/nano9121770.

[46] Modafferi V, Triolo C, Fiore M, Palella A, Spadaro L, Pianta N, et al. Effect of hematite doping with aliovalent impurities on the electrochemical performance of α-Fe_2O_3@rGO-based anodes in sodium-ion batteries. Nanomaterials 2020;10:1588. https://doi.org/10.3390/nano10081588.

[47] Guo T, Liao H, Ge P, Zhang Y, Tian Y, Hong W, et al. Fe_2O_3 embedded in the nitrogen-doped carbon matrix with strong C-O-Fe oxygen-bridge bonds for enhanced sodium storages. Mater Chem Phys 2018;216:58–63. https://doi.org/10.1016/j.matchemphys.2018.05.054.

[48] Qiang Z, Chen Y-M, Gurkan B, Guo Y, Cakmak M, Cavicchi KA, et al. Cooperatively assembled, nitrogen-doped, ordered mesoporous carbon/iron oxide nanocomposites for low-cost, long cycle life sodium-ion batteries. Carbon 2017;116:286–93. https://doi.org/10.1016/j.carbon.2017.01.093.

[49] Li M, Ma C, Zhu Q-C, Xu S-M, Wei X, Wu Y-M, et al. Well-ordered mesoporous Fe_2O_3/C composites as high performance anode materials for sodium-ion batteries. Dalton Trans 2017;46:5025–32. https://doi.org/10.1039/C7DT00540G.

[50] Soundharrajan V, Alfaruqi MH, Lee S, Sambandam B, Kim S, Kim S, et al. Multidimensional $Na_4VMn_{0.9}Cu_{0.1}(PO_4)_3$/C cotton-candy cathode materials for high energy Na-ion batteries. J Mater Chem A 2020;8:12055–68. https://doi.org/10.1039/D0TA03767B.